

Diffusion and operator entanglement spreading

Vincenzo Alba¹

¹*Institute for Theoretical Physics, Universiteit van Amsterdam,
Science Park 904, Postbus 94485, 1098 XH Amsterdam, The Netherlands*

Understanding the spreading of the *operator space entanglement entropy* (*OSEE*) is key in order to explore out-of-equilibrium quantum many-body systems. Here we argue that for integrable models the dynamics of the *OSEE* is related to the diffusion of the operator front. We derive the logarithmic bound $1/2 \ln(t)$ for the *OSEE* of some simple, i.e., low-rank, diagonal local operators. We numerically check that the bound is saturated in the rule 54 chain, which is representative of interacting integrable systems. Remarkably, the same bound is saturated in the spin-1/2 Heisenberg *XXZ* chain. Away from the isotropic point and from the free-fermion point, the *OSEE* grows as $1/2 \ln(t)$, irrespective of the chain anisotropy, suggesting universality. Finally, we discuss the effect of integrability breaking. We show that strong finite-time effects are present, which prevent from probing the asymptotic behavior of the *OSEE*.

I. INTRODUCTION

Understanding operator spreading in quantum many-body systems poses several intriguing challenges. Given an initially local-in-space operator \mathcal{O} , its dynamics under a many-body Hamiltonian H is $\mathcal{O}(t) = e^{iHt} \mathcal{O} e^{-iHt}$. The support of the operator increases with time, and the initially local information spreads within an emerging light-cone. The most urging question is as to whether a generic local operator admits an efficient representation as a Matrix Product Operator [1–6] (MPO). An affirmative answer would suggest that it is possible to simulate operator spreading with classical computers, with tremendous implications for Noisy Intermediate-Scale Quantum [7] (NISQ) computing technologies. A figure of merit for the MPO-simulability is the so-called *Operator Space Entanglement Entropy* (*OSEE*), which is the entanglement entropy in operator space.

Since its inception [8], the *OSEE* is attracting flourishing interest [5, 6, 8–11]. It has been suggested in Ref. 4 that in integrable systems the *OSEE* grows at most logarithmically with time, as it was found for free fermions [10]. Very recently, a logarithmic bound has been derived for the so-called rule 54 chain [12], which is believed to be representative of generic integrable systems. This has been checked in spin chains [12]. Oppositely, it has been argued that the *OSEE* grows linearly [10] in generic systems. Interestingly, this linear growth is predicted by the random unitary scenario, which posits that universal out-of-equilibrium features of the *OSEE* can be captured by replacing the evolution operator e^{iHt} with random unitary gates [13–17]. Despite all these efforts, however, the general mechanism behind the dynamics of the *OSEE* is yet to be unveiled, even for integrable systems. This is in contrast with the entanglement of a state, for which a powerful quasiparticle picture [18–21] explains the entanglement dynamics in terms of the ballistic motion of entangled quasiparticles.

One goal of this paper is to show that for generic integrable systems the *OSEE* reflects the diffusion of the operator front. Here, building on Ref. 12 we provide a

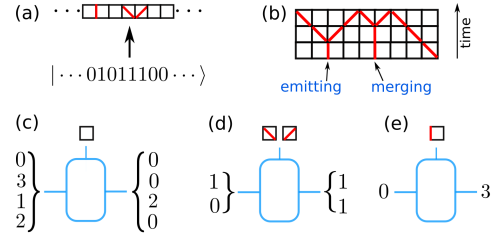


FIG. 1. Rule 54 chain. (a) Mapping to soliton space. Slanted lines and vertical lines are moving solitons and scattering ones. (b) Scattering solitons are time-delayed and can be “merging” or “emitting”. (c-e) MPO representation of the identity. Large boxes denote the tensors $A_{\beta_x, \beta_{x+1}}^{\tau_x}$ at site x . The physical index τ_x (vertical leg) takes values in soliton space. The allowed values of the virtual indices (horizontal legs) β_x, β_{x+1} are reported.

tight logarithmic bound for the *OSEE* of some simple operators in the rule 54 chain. Remarkably, the same bound is saturated in the spin-1/2 *XXZ* chain, at least away from the free-fermion point and the isotropic *XXX* point. This suggests a universal relation between diffusive and *OSEE* dynamics. Finally, we numerically investigate how this scenario is affected by integrability-breaking interactions.

To define the *OSEE* $S(\mathcal{O})$ we bipartite the system as $A \cup B$, and consider the Schmidt decomposition of \mathcal{O} as $\mathcal{O} / \sqrt{\text{Tr}(\mathcal{O}^\dagger \mathcal{O})} = \sum_i \sqrt{\lambda_i} \mathcal{O}_{A,i} \otimes \mathcal{O}_{B,i}$, with $\mathcal{O}_{A/B,i}$ two orthonormal bases for the operators with support in A and B , and $\lambda_i > 0$ the so-called Schmidt coefficients. The operator entanglement is $S(\mathcal{O}) = -\sum_i \lambda_i \ln \lambda_i$.

II. OSEE IN THE RULE 54 CHAIN

Here we focus on the *OSEE* spreading in the rule 54 chain [22]. The Hilbert space is that of a system of qubits $s_x = 0, 1$. The dynamics is generated by a three-site unitary gate U_x acting as

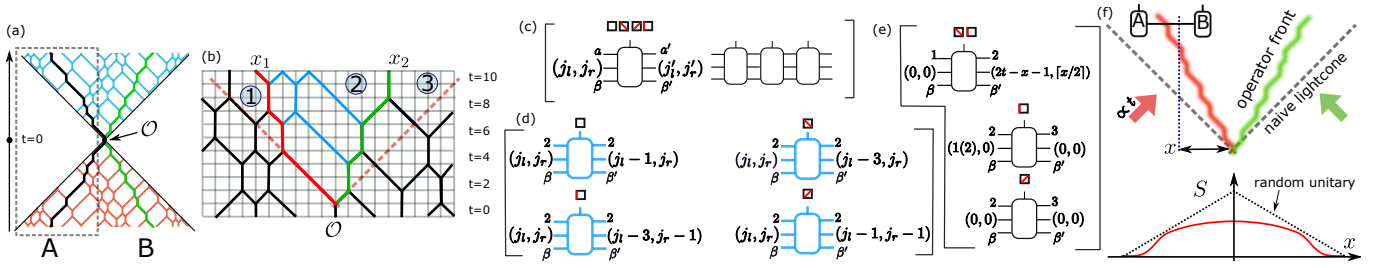


FIG. 2. (a) Dynamics of a diagonal operator \mathcal{O} in the rule 54. (a) Double lightcone. $\mathcal{O}(0)$ creates a pair of scattering left/right movers $x = 0$. They scatter with the background solitons. The upper and the lower half-lightcones coincide. (b) Typical evolution. Solitons positions x_1, x_2 are measured from the left edge of the light-cone (dashed line). Three different regions appear. Region 2 is the “reduced lightcone”. (c) MPO representation for $\mathcal{O}(t)$. Index $a = 1, 2, 3$ denotes the three regions in (b). The composite index (j_l, j_r) with $j_l, j_r \in [1, t]$ tracks the positions of the two solitons, and β, β' are as in Fig. 1. In 1 and 3, \mathcal{O} is the identity, and $a = a' = 1, 3$ and $j_l = j'_l = j_r = j'_r = 0$. An example of MPO contraction is shown. (d) MPO in region 2. All nonzero tensor elements are shown. (e) Tensors at the interface between different regions. At 1, 2 one has a left mover and $(j_l, j_r) = (2t - x - 1, \lceil x/2 \rceil)$. At 1, 3 the right mover that emerged at the center is found. (f) Cartoon for OSEE spreading in integrable systems (top). The operator front spreads with the dressed velocity v_d , implying that a number $\propto t$ of left and right moving solitons are present in the lightcone. The bipartition as $A \cup B$ with $A = [-t, x]$ is shown. The OSEE reflects the number of ways of distributing between A and B the solitons that are present in the lightcone. The effective MPO describing \mathcal{O} is reported. The virtual indices of the grouped tensors for A and B take values $\min(t - x, t + x)$, corresponding to the maximum number of solitons that can be stored in the smaller of the two subsystems. As a result the entanglement profile as a function of the cut position exhibits a “pancake” structure (see bottom), as opposed with the random-unitary scenario, which gives a “pyramid” profile (dotted profile).

$$U_x = |s_{x-1}, s'_x, s_{x+1}\rangle \langle s_{x-1} s_x, s_{x+1}|, \quad (1)$$

where $s'_x = s_{x-1} + s_{x+1} - s_{x-1}s_{x+1}$. U_x flips the qubit at x if one of the neighbouring qubits is 1. Any qubit configuration is evolved as $U = \prod_{\text{even } x} \prod_{\text{odd } x} U_x$. The rule 54 chain possesses well-defined quasiparticles, which is the key property of integrable systems. Quasiparticles are emergent left/right moving solitons. They correspond to pairs of adjacent qubits that are in the 1 state (more details are reported in Appendix C). Crucially, solitons undergo pairwise elastic scattering, which is implemented as a Wigner time delay [23] (cf. Fig. 1). Again, this is also generic for integrable models (see Ref. 25). Two solitons that are scattering correspond to the qubit configuration 010. The mapping between qubits and left/right movers is encoded as an MPO with bond dimension $\chi = 4$. Here we work directly in soliton space. As it is shown in Figure 1, a site x can be empty (empty box), or occupied by a left (right) mover (boxes with slanted lines in the Figure) if $(-1)^{x+t} = -1(1)$, or by two scattering solitons (vertical lines). If $(-1)^{x+t} = -1$ the two (“emitting”) solitons will reappear at time $t + 1$, whereas if $(-1)^{x+t} = 1$ the (“merging”) solitons will reappear at $t + 2$, reflecting the Wigner delay. We are interested in the Heisenberg dynamics of local operators. Let us first consider the identity operator $\mathbf{1} = \prod_{x=0}^{L-1} \sum_{s_x} |s_x\rangle \langle s_x|$ in soliton space. As for all diagonal operators, one can consider the evolution of the ket or bra separately, because they evolve in the same way under application of U and U^\dagger . One now has the evolution of the “flat” superposition $\prod_x \sum_{s_x} |s_x\rangle$. In soliton space this maps to the flat superposition of all allowed soliton configurations. This

is efficiently encoded as an MPO (see Appendix C) as $\mathbf{1} = \sum_{\{\beta_x\}} \prod_i A_{\beta_x, \beta_{x+1}}^{\tau_x} |\tau_x\rangle \langle \tau_x|$. Here $A_{\beta_x, \beta_{x+1}}^{\tau_x}$ is a tensor living on site x . The index τ_x labels the soliton configuration, $\beta_x \in [0, \chi]$ are the virtual indices, with χ the bond dimension. Here $A_{\beta_x, \beta_{x+1}}^{\tau_x} = 1$ only for the cases shown in Fig. 1 (c-e), and it is zero otherwise. The role of β_x is to enforce some kinematic constraints, for instance, that a left mover is followed only by a right mover or by an empty site (see Fig. 10 in Appendix C). Since χ is small and the identity operator does not evolve, one has that $S(\mathbf{1})$ is constant in time.

This changes dramatically for the OSEE of a local operator. By adapting a remarkable result of Ref. 26 it has been shown [12] that the dynamics of operators is described by an MPO with $\chi \propto t^2$. This implies the “naive” bound $S(\mathcal{O}) \leq 2 \ln(t)$ for the OSEE. Here we show that the growth of the OSEE reflects the fluctuations of the number of solitons between A and its complement. This allows us to derive a tighter bound for the OSEE spreading. To derive our result, we review the construction of the MPO for the diagonal operator that inserts two scattering solitons at $L/2$, i.e., $\mathcal{O} = |010\rangle \langle 010|$. This is illustrated in Fig. 2. \mathcal{O} is diagonal, implying that the upper and the lower lightcones coincide. At $t > 0$ a left and right movers are emitted from $L/2$. They play a crucial role in the MPO construction. Indeed, $\mathcal{O}(t)$ corresponds to the flat superposition of all the possible soliton configurations that contain the left and right movers that were inserted at the origin at $t = 0$. This simple constraint on the soliton configurations implies that the OSEE grows logarithmically.

We note that as the solitons emitted from the center scatter with the background solitons, they undergo two

biased random walks. Their positions $x_1, x_2 = 0, 1, \dots$ at time t , which are measured from the left edge of the lightcone (dashed lines in Fig. 2 (b)), are determined by the scatterings. The crucial observation is that all the background solitons that scattered with the two solitons emitted from the center are contained in the “reduced lightcone” within them (region 2 in Fig. 2 (b)). Outside of the reduced lightcone $\mathcal{O}(t)$ is the identity. To construct the MPO for $\mathcal{O}(t)$ we complement the MPO for the identity in Fig. 1 with some extra indices. First, we introduce an index $a = 1, 2, 3$ to keep track of the different regions. The number of left/right movers in region 2 is tracked by two extra indices j_l, j_r . Finally, the index β is as in Fig. 1. The structure of the MPO is summarised in Fig. 2 (c). Physically, j_r at (x, t) counts the number of right movers in region 2, whereas j_l is the expected distance between x and the right mover that emerged from the center, assuming that there are no left movers in the remaining interval $[x + 1, t]$ of the lightcone. In regions 1, 3 we set $a = a' = 1, 3$, and $j_l = j'_l = j_r = j'_r = 0$. The allowed values of j_l, j_r in region 2 for which the MPO is nonzero are reported in Fig. 2 (d). The interpretation is straightforward. For instance, if at site x there is no soliton, one has $j'_r = j_r$ and $j'_l = j_l - 1$, because the distance from the right mover emerged from the center decreases by one after moving to the next site. If at x there is a right mover, then $j'_r = j_r - 1$. If a left mover is present, one has that $j'_l = j_l - 3$ because the left mover shifts the right mover emerging from the center by two sites to the left (see Fig. 2 (b)). Finally, Fig. 2 (e) shows the tensors at the interface between regions 1, 2 and 2, 3. At the boundary 1, 2 a left mover is present, and j_l, j_r is initialized as $j_r = \lceil x_1/2 \rceil$ and $j_l = 2t - x_1 - 1$. At the boundary 2, 3 one has $j_l = j'_l = 0$, ensuring that all the background solitons expected within the reduced lightcone have been found and the right mover that emerged from the center is on that site. Notice that there is a subtlety due to the kinematics of solitons if two scattering solitons are met at 2, 3 (see Fig. 2 (e)). This, however, does not affect the leading logarithmic growth of the *OSEE*. Now, since $0 \leq j_l, j_r \leq t$, the bond dimension of the MPO that describes $\mathcal{O}(t)$ is clearly $\chi \propto t^2$, implying that $S \leq 2 \ln(t)$. To proceed, we observe that due to the scatterings, the left and right movers that emerged from the center move with a “dressed” velocity [27, 28] $v_d = 1/2$ (the bare velocity is $v_b = 1$). Crucially, their trajectories, and the operator front, exhibit diffusion [28, 29]. This diffusion is essential to have nonzero entanglement. Indeed, the dressed solitons behave as free particles, their trajectories cross each other. This implies that a flat superposition of dressed solitons is mapped onto itself by the dynamics, which implies the absence of entanglement production.

We now observe that in the reduced lightcone there are $\propto t$ left/right movers. Let us consider the bipartition $A \cup B = [-t, x] \cup [x, t]$, with $x \leq 0$. A crude approximation

for $\mathcal{O}(t)$ gives

$$\mathcal{O}(t) = \sum_{k=0}^{t-|x|} \frac{\sqrt{\binom{t-|x|}{k} \binom{t+|x|}{t-k}}}{\sqrt{\binom{2t}{t}}} \mathcal{O}_k^A \otimes \mathcal{O}_{t-k}^B. \quad (2)$$

Here \mathcal{O}_k^A and \mathcal{O}_{t-k}^B are normalised operators in A and B constructed with k and $t - k$ solitons. In (2) we assume that \mathcal{O}_k^A and \mathcal{O}_{t-k}^B are some “flat” superpositions of all the configurations with k and $t - k$ solitons, i.e., we assume that the positions of the background solitons are maximally “scrambled” within the reduced lightcone. This is not true in general because solitons scatter locally. We also assume that \mathcal{O}_k^A and \mathcal{O}_{t-k}^B form orthonormal bases for A and B . The two binomials in the sum in (2) give the number of ways of arranging the solitons in the two subsystems. Note that for large t the behavior of (2) is dominated by the configurations with $k = (t - |x|)/2$, showing a spreading \sqrt{t} . This reflects that there is an average number $(t - |x|)/2$ of solitons in subsystem A . The number of solitons in A fluctuates, the fluctuations being $\propto \sqrt{t}$. We anticipate that these fluctuations are responsible for the growth of the *OSEE*. Crucially, this mechanism is different from the spreading of the state entanglement after a global quantum quench, where entanglement is produced locally at each point in space and it is transported by entangled multiplets of quasiparticles [18–20]. This is also different from the random-unitary scenario. The main assumption of this scenario is that the entanglement profile $S(x, t)$ satisfies the equation $\partial_t S = \Gamma(\partial_x S)$. Here Γ is the entropy production rate, which depends on the spatial variation of the entropy profile, and it is nonzero at any point in space. This implies that the entanglement profile has the typical “pyramid” shape (Fig. 2 (f)). In contrast, the logarithmic growth in integrable systems is reflected in a “pancake” structure in the entanglement profile (Fig. 2 (f), see also Appendix B).

We can now derive a bound on the *OSEE* growth from (2). The bond dimension of the decomposition from (2) is $t - |x| + 1$. Note that $t - |x|$ is the largest number of solitons that can be accommodated within A . The eigenvalues of the reduced density matrix for A are simply $\lambda_k = \binom{t-|x|}{k} \binom{t+|x|}{t-k} / \binom{2t}{t}$. Notice that the fact that there are only $\propto t$ eigenvalues is an approximation. In the rule 54 chain one should expect $\propto t^2$ nonzero eigenvalues, instead of the $\propto t$ predicted by the argument above. On the other hand, the number $\propto t^2$ does not imply the scaling $2 \ln(t)$ for the *OSEE* because the eigenvalues are not equal but exhibit a nontrivial distribution. By using the explicit form of λ_k one obtains the analytical bound for the *OSEE* as (see Ref. 30 for a similar calculation)

$$S_{\max} = \frac{1}{2} \ln(t). \quad (3)$$

Crucially, the prefactor 1/2 in (3) is reminiscent of the \sqrt{t} fluctuations in the number of solitons in the subsystems A and B . Eq. (3) is expected to hold for the

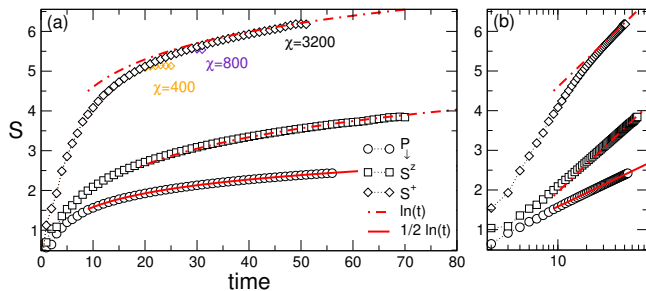


FIG. 3. (a) Operator entanglement in the rule 54 chain. Different symbols are $tDMRG$ data for $P_{\downarrow} \equiv (1/2 - S^z)$ (circles), S^z (squares), and S^+ (diamonds), inserted at the chain center. The continuous and dashed-dotted lines are $S_{\max} = 1/2 \ln(t)$, and $2S_{\max}$, respectively. (b) Same data as in (a) using a logarithmic scale on the x -axis.

simple, i.e., low-rank, diagonal operator. We should remark that the prefactor of the $OSEE$ growth should depend on the structure of the operator. For instance, the identity operator, for which the $OSEE$ is constant in time, is $\mathbf{1} = P_{\downarrow} + P_{\uparrow}$. On the other hand, the $OSEE$ of $S_z = P_{\uparrow} - P_{\downarrow}$ grows logarithmically. Moreover, (see Ref. 16) for traceful operators, the prefactor of the $OSEE$ growth depends on the trace. Also, for off-diagonal operators (see Fig. 2 (a)) the upper and lower lightcones do not coincide, suggesting a faster growth of the $OSEE$.

We should also stress that the behavior of the $OSEE$ in free-fermion systems is different from (3). For instance, the $OSEE$ of S^z saturates, whereas that of S^x increases as $1/3 \ln(t)$. Interestingly, the prefactor $1/3$ could reflect the absence of diffusion for free fermions, suggesting that the $OSEE$ could be potentially useful to distinguish interacting integrable from free systems [31].

III. INTEGRABLE DYNAMICS: RULE 54 AND XXZ SPIN CHAIN

To benchmark our main result (3), in Fig. 3 we discuss the case of the rule 54 chain. We focus on the projector operator $P_{\downarrow} \equiv (1/2 - S^z)$, the raising operator S^+ , and S^z , all inserted at the center of the chain. The symbols are $tDMRG$ data [32–34]. For S^+ , we report the bond dimension χ . The full line is Eq. (3), whereas the dashed-dotted line is $2S_{\max}$. The agreement between (3) and the data is excellent for P_{\downarrow} , signalling that the bound (3) is saturated. For S^z one should also expect $S = 2S_{\max}$ (see Ref. 16). A fit to $\kappa \ln(t) + a$ gives $\kappa \approx 0.9$. For S^+ , we observe a reasonable agreement with $2S_{\max}$, although finite-time effects seem larger.

We now discuss the universality of (3). We consider a generalisation of the spin-1/2 XXZ chain defined by the

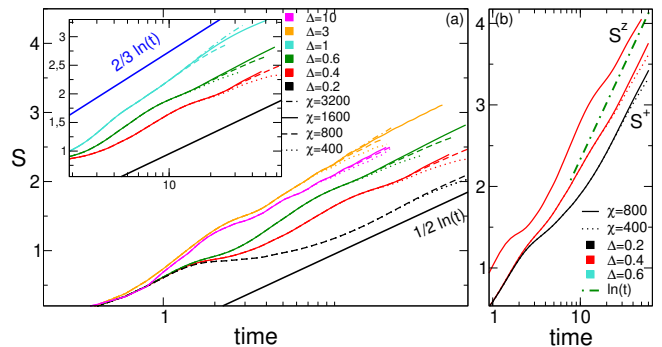


FIG. 4. $OSEE$ in the XXZ chain. (a) $tDMRG$ data for $P_{\downarrow} \equiv (1/2 - S^z)$ for several values of Δ . Different line styles are different bond dimensions χ . For $\Delta \neq 1$ data are compatible with S_{\max} . For $\Delta = 1$ (inset) the $OSEE$ shows a faster growth. (b) Dynamics of the $OSEE$ of S^+ and S^z .

Hamiltonian

$$H = \sum_{i=1}^L \frac{1}{2} (S_i^+ S_{i+1}^- + S_i^- S_{i+1}^+) + \Delta \sum_{i=1}^L S_i^z S_{i+1}^z + \Delta' \sum_{i=1}^L S_i^z S_{i+2}^z \quad (4)$$

where Δ, Δ' are real parameters. For $\Delta' = 0$ the model is integrable for any Δ , whereas $\Delta' \neq 0$ breaks integrability (see Appendix A). Let us consider the integrable case, i.e., $\Delta' = 0$. We discuss the $OSEE$ of P_{\downarrow} in Fig. 4 (a) and that of S^+ and S^z in Fig. 4 (b). The $tDMRG$ data for P_{\downarrow} exhibit a clear logarithmic increase. For $\Delta \neq 1$ they are compatible with $S_{\max} + c(\Delta)$, suggesting universality of the prefactor $1/2$ of the $OSEE$. Interestingly, $c(\Delta)$ reflects the behavior of the diffusion constant [35, 36], i.e., it increases with Δ for $0 \leq \Delta \leq 1$, then it decreases for $\Delta > 1$, saturating for $\Delta \rightarrow \infty$. For $\Delta \rightarrow 1$ the diffusion constant diverges [35, 36], which signals superdiffusive behavior, suggesting violations of (3) for $\Delta = 1$. The data in the inset of Fig. 4 might suggest the behavior $\kappa \ln(t)$ with $k > 1/2$, although they could just signal large finite-time corrections. It has been proposed in Ref. 37 that the superdiffusive behavior as $t^{2/3}$ arises at $\Delta = 1$, suggesting $S \propto 2/3 \ln(t)$ (reported for comparison in Fig. 4). Finally, in Fig. 4 (b) we discuss S^z and S^+ . The $OSEE$ increases faster. Finite-time effects are large, and the evidence for the behavior $S \propto 2S_{\max}$ is weak.

IV. NON-INTEGRABLE DYNAMICS

The soliton picture should breakdown for generic models, because they do not possess quasiparticles. According to the random-unitary scenario, this would imply a linear growth of the $OSEE$. However, it has been suggested in Ref. 38 that if a conservation law is present, the Rényi operator entanglement $S^{(2)}$ of the associated local

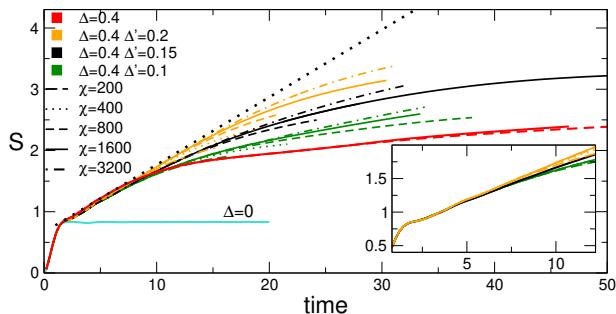


FIG. 5. *OSEE* dynamics and integrability breaking: *OSEE* of $P_{\downarrow} \equiv (1/2 - S^z)$ inserted at the center of the chain. Lines are *tDMRG* data for the *XXZ* chain with $\Delta = 0.4$ and several values of Δ' . Different bond dimensions χ are shown. We also show the data for $\Delta = \Delta' = 0$, i.e., the free-fermion point, where the *OSEE* saturates. The dotted line is $S \simeq 0.11t + 0.66$, and it is obtained by fitting the approximately linear behavior at intermediate times. The inset is a zoom for $t \leq 10$.

operator exhibits logarithmic growth, even if the system is nonintegrable. Notice that for systems without conservation laws, for instance Floquet systems, the linear growth of operator entanglement is supported by exact calculations [39–41]. Our *tDMRG* results for P_{\downarrow} are in Fig. 5. It is enlightening to first consider the integrable case for $\Delta' = 0$ and $\Delta = 0.4$. At very short times $t \approx 2$, the *OSEE* exhibits a jump, reflecting that at $\Delta = 0$ the *OSEE* saturates (see the result for $\Delta = 0$ in the Figure). Then, there is an intermediate regime, where a nearly-linear growth is present. The asymptotic behavior sets in at longer times. Upon breaking integrability *tDMRG* simulations become more challenging. At short times a linear increase is observed. However, this could be reminiscent of the transient regime also observed for $\Delta' = 0$. In fact, a change in behavior happens at $t^*(\Delta')$, with t^* increasing with Δ' . The data in Fig. 5 are compatible with two scenarios. In one scenario the *OSEE* increases linearly at asymptotically long times. The asymptotic regime sets in after a long transient in which the system behaves as if it was integrable. The prefactor of the linear growth should presumably increase with Δ' . Alternatively, the breaking of integrability gives rise to a longer transient, as compared with the integrable case, before the logarithmic behavior sets in. Longer transients should be expected generically for nonintegrable systems because transport is dominated by diffusion.

V. CONCLUSIONS

We have shown that in integrable systems the growth of the *OSEE* of some simple operators exhibits a logarithmic increase. Our work opens several research avenues. First, it would be important to derive *ab initio* the behavior in (3), at least in the rule 54 chain, for instance, by using the recent developments in Ref. 42 and

43. It is also important to understand the *OSEE* for more complicated operators and systems. Our data for non-integrable systems do not allow to reach a conclusion on the behavior of the *OSEE* in generic systems, although they are compatible with Ref. 38. It is of fundamental importance to clarify this issue. Finally, the argument leading to (3) gives that S_{\max} is the same for all the Rényi entropies $S^{(\alpha)}$. However, we numerically checked that although $S^{(\alpha)}$ exhibit logarithmic growth, the prefactor is smaller than $1/2$ and it depends on α . It would be interesting to clarify this issue by studying the Rényi entropies. Finally, it would be interesting to clarify the relationship between *OSEE* and anomalous transport, for instance superdiffusion [36, 44, 45].

ACKNOWLEDGMENTS

I am grateful to Jerome Dubail and Marko Medenjak for introducing me to the problem of operator entanglement and to the Bobenko chain, and for several important discussions. I would also like to thank Maurizio Fagotti and Bruno Bertini for several discussions. I acknowledge support from the European Research Council under ERC Advanced grant 743032 DYNAMINT.

Appendix A: Spectral diagnostic for the non-integrable case

Here we address the integrability of the hamiltonian (A1). We consider the general hamiltonian

$$H = H_{XXZ} + \sum_i \frac{J'}{2} (S_i^+ S_{i+2}^- + S_i^- S_{i+2}^+) + \Delta' \sum_i S_i^z S_{i+2}^z, \quad (\text{A1})$$

where H_{XXZ} is the standard Heisenberg *XXZ* hamiltonian

$$H_{XXZ} = \sum_i \frac{1}{2} (S_i^+ S_{i+1}^- + S_i^- S_{i+1}^+) + \Delta \sum_i S_i^z S_{i+1}^z. \quad (\text{A2})$$

For $J' = \Delta' = 0$ one recovers the *XXZ* chain, which is integrable by the Bethe ansatz for any Δ . To understand the effect of the integrability breaking terms we study the gaps δ_n between adjacent levels of the energy spectrum of (A1). Here we define δ_n as

$$\delta_n \equiv E_{n+1} - E_n, \quad (\text{A3})$$

with E_n energy levels. For chaotic systems the behavior of δ_n should be described by an appropriate random matrix ensemble, provided that the contribution of the density of states, which is model dependent, is removed. An alternative solution is to focus on the ratio between consecutive gaps r_n as [46].

$$0 \leq r_n \equiv \min\{\delta_n, \delta_{n-1}\} / \max\{\delta_n, \delta_{n-1}\} \leq 1. \quad (\text{A4})$$

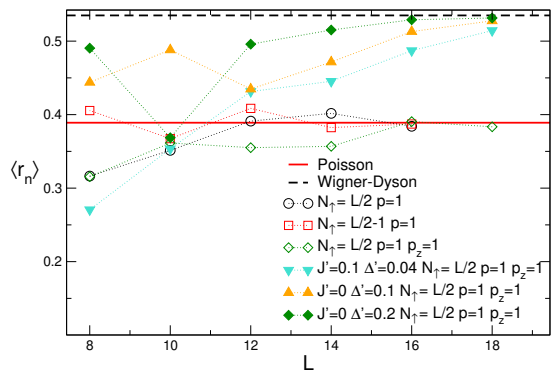


FIG. 6. Spectral diagnostics of integrability-breaking. The figure shows the ratio of consecutive gaps r_n (cf. (A4)) versus the system size L for the hamiltonian (A1). Here we focus on the case with $\Delta = 0.4$, and several J' and Δ' . The empty symbols are the data for the integrable case $J' = \Delta' = 0$. The different symbols correspond to different number of up spins (magnetization) N_\uparrow , spatial parity eigenvalue p , and spin inversion eigenvalue p_z . Only the quantum numbers that are fixed are reported in the legend. The full and dashed lines are the expected results for integrable and chaotic models.

For Poisson-distributed energy levels, i.e., for integrable systems, the average value of the ratio is $\langle r_n \rangle = 2 \ln(2) - 1 \approx 0.386$. In the non-integrable case one should expect that energy levels are described by the Gaussian Orthogonal Ensemble (*GOE*). This gives[47] $\langle r_n \rangle = 4 - 2\sqrt{3} \approx 0.535$. Our results are reported in Fig. 6. The data are obtained from exact diagonalisation of a chain with $L \leq 18$ sites. Periodic boundary conditions are used. In the Figure N_\uparrow is the number of up spins, which fixes the magnetization sector. Most of the data are at half-filling $N_\uparrow = L/2$, although we consider also $N_\uparrow = L/2 - 1$. We denote with $p = \pm 1$ the eigenvalue of the parity under reflection with respect to the center of the chain. Here $p_z = \pm 1$ is the eigenvalue of the spin inversion operator. Empty symbols are for the integrable case, i.e., the *XXZ* chain with $\Delta = 0.4$ (cf. (A2)). The different symbols are for different symmetry sectors. In the legend we only report the quantum numbers that are fixed. The results for the integrable case are reasonably close to the expected value $\langle r_n \rangle \approx 0.386$, at least in the limit $L \rightarrow \infty$.

This is different upon breaking integrability. The data are reported as full symbols in Fig. 6. First, one should stress that the Wigner-Dyson result $\langle r_n \rangle \approx 0.535$ is expected to hold in the limit $L \rightarrow \infty$ if one factors out all the conserved quantities. The down-triangle in the figure are the data for $J' = 0.1$ and $\Delta' = 0.04$. Clearly, finite-size corrections are present, although the data for the largest size $L = 18$ are converging to the expected result. The up triangles and the diamonds are the data for $J' = 0$ and $\Delta' = 0.1$ and $\Delta' = 0.2$, respectively. Upon increasing Δ' , the data approach the Wigner-Dyson result faster, as expected. Still, in both cases there is reasonable agreement with the random matrix result for $L = 18$. However, we should remark that, although the analysis

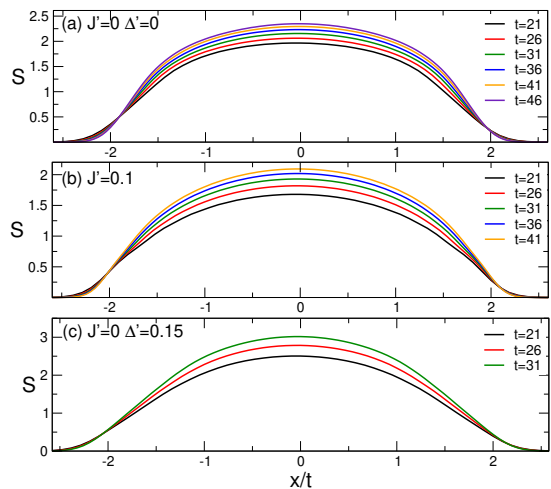


FIG. 7. Profile of the operator entanglement. The results are for $P_\downarrow \equiv 1/2 - S^z$ inserted at the center of the chain. The operator entanglement is plotted as a function of the rescaled position x/t , with x measured from the chain center and t the time. (a) shows the integrable case, i.e., the *XXZ* chain with $\Delta = 0.4$. In (b) and (c) we consider the nonintegrable deformation of the *XXZ*.

performed here suggests that for $\Delta' = 0.1, 0.2$ the hamiltonian (A1) is not integrable, it does not give any information on the time-scale after which the effect of the integrability-breaking interactions start to appear.

Appendix B: Entanglement profiles

Here we discuss the behavior of the spatial profile of the *OSEE* of the projector operator $P_\downarrow \equiv 1/2 - S^z$ in both integrable and non-integrable systems. The operator is inserted at the center of the chain. Our results are presented in Fig. 7. We consider the deformed *XXZ* chain hamiltonian in (A1). We fix $\Delta = 0.4$. In Fig. 7 (a) we focus on the integrable case $J' = 0$ and $\Delta' = 0$. The figure shows the *OSEE* plotted as a function of x/t , with x the distance from the center of the chain. Clearly, outside of the lightcone for $|x/t| > 2$ the *OSEE* vanishes. Within the lightcone, in the integrable case the entanglement profile exhibits a rather flat behavior. This is in contrast with the expected behavior in generic systems described by random unitaries, for which the *OSEE* has a maximum at $x = 0$ and decreases linearly with the distance from the center, exhibiting a “pyramid-like” structure.

In Fig. 7 (b) we consider the effect of the integrability breaking. We now fix $J' = 0.1$ and $\Delta' = 0$. An important observation is that since we are interested in the long time limit and the *OSEE* generically grows faster upon increasing the strength of the integrability-breaking terms we are limited to relatively weak integrability breaking. The entanglement profile is qualitative similar to the integrable case in Fig. 7 (a). A similar behavior is observed in the case with $J' = 0$ and $\Delta' = 0.15$ (see Fig. 7 (c)).

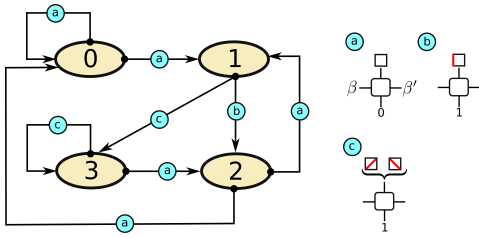


FIG. 8. MPO representation of the mapping between computational basis and the soliton basis in the rule 54 chain. The diagram shows the finite-state machine encoding the mapping. The possible states of the machine are labeled as $s = 0, 1, 2, 3$. The arrows denote transitions between different states. (a-c) Tensors forming the MPO. The lower indices take values 0, 1. The upper index can be the empty box (no solitons), slanted lines denoting left and right movers, and the vertical line, which corresponds to a pair of scattering solitons. The presence of the left and right mover depends on the combined parity of spatial position and time. The virtual indices β, β' for which the tensor is nonzero are the states of the machine connected by the tensor.

Appendix C: Solitonic machines

The mapping between the computational basis and the soliton basis for the rule 54 chain (see Fig. 1) is reported in Fig. 8 in the framework of finite-state machines. The possible states of the machine are $s = 0, 1, 2, 3$. These are the states that are explored by a machine that scans a bit configuration site by site proceeding from left to right. The internal states of the machine are determined by the bit configurations on nearest-neighbour sites. The goal of the machine is to identify pairs of consecutive 11, which correspond to left/right movers, and the configuration 010, which corresponds to two scattering solitons. Let us assume that the machine is at site x and that $s_x = s_{x-1} = 0$. This defines the internal state 0 of the machine. State 1 means that $s_x = 1$ and $s_{x-1} = 0$. State 2 is defined by the condition $s_x = 0$ and $s_{x-1} = 1$. Finally state 3 means that $s_x = s_{x-1} = 1$. All the transitions between the different states are reported in the diagram in Fig. 8. When the machine moves from x to $x + 1$ it gives as an output the soliton configuration on x . For instance, if the transition is $0 \rightarrow 0$ the only possibility is that on x there is no soliton. The possible transitions define all the nonzero elements of the tensors $A_{\beta, \beta'}^{s_x, \tau_x}$ forming the MPO that implements the mapping. Here $\beta, \beta' = 0, 1, 2, 3$ are the virtual indices of the MPO, whereas s_x and τ_x are

the physical indices taking values in the bit space and in the soliton space, respectively.

From the mapping in Fig. 9 one can read out all the possible solitonic configurations on L sites. The machine generating them gives the MPO representation of the identity operator in soliton space. The MPO representing the identity, or, equivalently the infinite temperature state in the space of solitons is shown in Fig. 9. The meaning of the machine states is not the same as in Fig. 8.

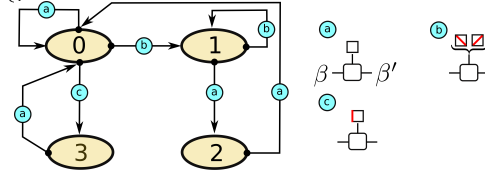


FIG. 9. Soliton machine that generates the MPO representation of the identity operator (infinite-temperature state). In (a-c) we report the tensors forming the MPO representation. The virtual indices of the tensor have values in the space of the machine states $\beta, \beta' = 0, 1, 2, 3$.

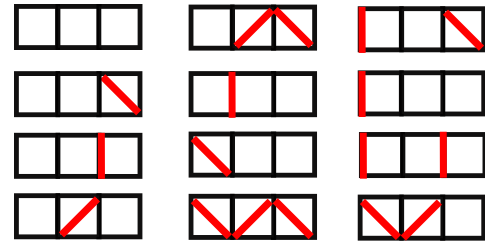


FIG. 10. All the possible solitonic configurations on a system with $L = 3$ sites. The configurations are obtained by using the MPO representation of the identity in Fig. 9.

Now state 0 means that at site x there is no solitons and on $x - 1$ there were no free left and right movers (slanted lines). State 1 means that on x there is a left/right mover. State 2 is defined by the condition that on x there is no soliton and a left/right mover is present at $x - 1$. Finally, state 3 means that on site x there is a pair of scattering solitons (vertical line). Note that the presence of state 2 imposes some kinematic constraint for the solitons, i.e., that a left and right mover has to be followed by at least two empty boxes. To illustrate the solitonic patterns that correspond to the identity, in Fig. 10 we report all the solitonic configurations that are allowed on three sites.

-
- [1] M. Zwolak and G. Vidal, Mixed-State Dynamics in One-Dimensional Quantum Lattice Systems: A Time-Dependent Superoperator Renormalization Algorithm, *Phys. Rev. Lett.* **93**, 207205 (2004).
 [2] F. Verstraete, J. J. García-Ripoll, and J. I. Cirac, Matrix Product Density Operators: Simulation of Finite-

- Temperature and Dissipative Systems, *Phys. Rev. Lett.* **93**, 207204 (2004).
 [3] M. B. Hastings, Solving gapped Hamiltonians locally, *Phys. Rev. B* **73**, 085115 (2006).
 [4] T. Prosen and M. Znidaric, Is the efficiency of classical simulations of quantum dynamics related to integrabil-

- ity?, *Phys. Rev. E* **75**, 015202(R) (2007).
- [5] M. Znidarič, T. Prosen, and I. Pizorn, Complexity of thermal states in quantum spin chains, *Phys. Rev. A* **78**, 022103 (2008).
- [6] A. Molnar, N. Schuch, F. Verstraete, and J. I. Cirac, Approximating Gibbs states of local Hamiltonians efficiently with projected entangled pair states, *Phys. Rev. B* **91**, 045138 (2015).
- [7] J. Preskill, Quantum Computing in the NISQ era and beyond, *Quantum* **2**, 79 (2018).
- [8] P. Zanardi, Entanglement of quantum evolutions, *Phys. Rev. A* **63**, 040304(R) (2001).
- [9] J. Dubail, Entanglement scaling of operators: a conformal field theory approach, with a glimpse of simulability of long-time dynamics in $1+1d$, *J. Physics A* **50**, 234001 (2017).
- [10] I. Pizorn and T. Prosen, Operator space entanglement entropy in XY spin chains, *Phys. Rev. B* **79**, 184416 (2009).
- [11] M. J. Hartmann, J. Prior, S. R. Clark, and M. B. Plenio, Density Matrix Renormalization Group in the Heisenberg Picture, *Phys. Rev. Lett.* **102**, 057202 (2009).
- [12] V. Alba, J. Dubail, and M. Medenjak Operator Entanglement in Interacting Integrable Quantum Systems: the Case of the Rule 54 Chain, *Phys. Rev. Lett.* **122**, 250603 (2019).
- [13] A. Nahum, J. Ruhman, S. Vijay, and J. Haah, Quantum entanglement growth under random unitary dynamics, *Phys. Rev. X* **7**, 031016 (2017).
- [14] A. Nahum, S. Vijay, and J. Haah, Operator Spreading in Random Unitary Circuits, *Phys. Rev. X* **8**, 021014 (2018).
- [15] C. W. von Keyserlingk, T. Rakovszky, F. Pollmann, and S. L. Sondhi, Operator Hydrodynamics, OTOCs, and Entanglement Growth in Systems without Conservation Laws, *Phys. Rev. X* **8**, 021013 (2018).
- [16] C. Jonay, D. Huse, and A. Nahum, Coarse-grained dynamics of operator and state entanglement, [arXiv:1803.00089](https://arxiv.org/abs/1803.00089).
- [17] V. Khemani, A. Vishwanath, and D. A. Huse, Operator Spreading and the Emergence of Dissipative Hydrodynamics under Unitary Evolution with Conservation Laws, *Phys. Rev. X* **8**, 031057 (2018).
- [18] P. Calabrese and J. Cardy, Evolution of Entanglement Entropy in One-Dimensional Systems, *J. Stat. Mech.* (2005) P04010.
- [19] M. Fagotti and P. Calabrese, Evolution of entanglement entropy following a quantum quench: Analytic results for the XY chain in a transverse magnetic field, *Phys. Rev. A* **78**, 010306 (2008).
- [20] V. Alba and P. Calabrese, Entanglement and thermodynamics after a quantum quench in integrable systems, *PNAS* **114**, 7947 (2017).
- [21] V. Alba, P. Calabrese, *SciPost Phys.* **4**, 017 (2018)
- [22] A. Bobenko, M. Bordemann, C. Gunn, and U. Pinkall, On two integrable cellular automata, *Commun. Math. Phys.* **158**, 127 (1993).
- [23] E. P. Wigner, Lower Limit for the Energy Derivative of the Scattering Phase Shift, *Phys. Rev.* **98**, 145 (1955)
- [24] see Supplemental Material.
- [25] B. Doyon, T. Yoshimura, and J.-S. Caux, Soliton Gases and Generalized Hydrodynamics, *Phys. Rev. Lett.* **120**, 045301 (2018)
- [26] K. Klobas, M. Medenjak, T. Prosen, and M. Vanicat, Time-Dependent Matrix Product Ansatz for Interacting Reversible Dynamics, *Commun. Math. Phys.* **371**, 651 (2019).
- [27] Operator growth and eigenstate entanglement in an interacting integrable Floquet system S. Gopalakrishnan, *Phys. Rev. B* **98**, 060302(R) (2018).
- [28] S. Gopalakrishnan, D. A. Huse, V. Khemani, and R. Vasseur, Hydrodynamics of operator spreading and quasiparticle diffusion in interacting integrable systems, *Phys. Rev. B* **98**, 220303 (2018).
- [29] J. De Nardis, D. Bernard, and B. Doyon, Hydrodynamic Diffusion in Integrable Systems, *Phys. Rev. Lett.* **121**, 160603 (2018).
- [30] M. Kiefer-Emmanouilidis, R. Unanyan, J. Sirker, and M. Fleischhauer, Bounds on the entanglement entropy by the number entropy in non-interacting fermionic systems, [arXiv:2003.03112](https://arxiv.org/abs/2003.03112).
- [31] H. Spohn, Interacting and noninteracting integrable systems, *J. Math. Phys.* **59**, 091402 (2018).
- [32] U. Schollwöck, The density-matrix renormalization group in the age of matrix product states, *Annals of Physics* **326**, 96 (2011).
- [33] S. Paeckel, T. Köhler, A. Swoboda, S. R. Manmana, U. Schollwöck, and C. Hubig, Time-evolution methods for matrix-product states, *Annals of Physics* **411**, 167998 (2019).
- [34] Simulations are performed by using the ITensor library, itensor.org.
- [35] E. Ilievski, J. De Nardis, M. Medenjak, and T. Prosen, Superdiffusion in One-Dimensional Quantum Lattice Models, *Phys. Rev. Lett.* **121**, 230602 (2018).
- [36] S. Gopalakrishnan and R. Vasseur, Kinetic Theory of Spin Diffusion and Superdiffusion in XXZ Spin Chains, *Phys. Rev. Lett.* **122**, 127202 (2019).
- [37] M. Ljubotina, M. Žnidarič, and T. Prosen, Spin diffusion from an inhomogeneous quench in an integrable system, *Nature Communications* **8**, 16117 (2017).
- [38] D. Muth, R. G. Unanyan, and M. Fleischhauer, Dynamical Simulation of Integrable and Nonintegrable Models in the Heisenberg Picture, *Phys. Rev. Lett.* **106**, 077202 (2011).
- [39] B. Bertini, P. Kos, and T. Prosen, Entanglement Spreading in a Minimal Model of Maximal Many-Body Quantum Chaos, *Phys. Rev. X* **9**, 021033 (2019).
- [40] B. Bertini, P. Kos, and T. Prosen, Operator Entanglement in Local Quantum Circuits I: Chaotic Dual-Unitary Circuits, *SciPost Phys.* **8**, 067 (2020).
- [41] B. Bertini, P. Kos, and T. Prosen, Operator Entanglement in Local Quantum Circuits II: Solitons in Chains of Qubits, *SciPost Phys.* **8**, 068 (2020).
- [42] K. Klobas and T. Prosen, Space-like dynamics in a reversible cellular automaton, [arXiv:2004.01671](https://arxiv.org/abs/2004.01671).
- [43] K. Klobas, M. Vanicat, J. P. Garrahan, and T. Prosen, Matrix product state of multi-time correlations, *J. Phys. A* **10**, 1088 (2020).
- [44] M. Dupont and J. E. Moore, Universal spin dynamics in infinite-temperature one-dimensional quantum magnets, *Phys. Rev. B* **101**, 121106(R) (2020).
- [45] J. De Nardis, M. Medenjak, C. Karrasch, and E. Ilievski, Universality Classes of Spin Transport in One-Dimensional Isotropic Magnets: The Onset of Logarithmic Anomalies, *Phys. Rev. Lett.* **124**, 210605 (2020).
- [46] V. Oganesyan and D. Huse, Localization of interacting fermions at high temperature, *Phys. Rev. B* **75**, 155111 (2007).

- (2007).
- [47] Y. Y. Atas, E. Bogomolny, O. Giraud, and G. Roux, The distribution of the ratio of consecutive level spacings in random matrix ensembles, *Phys. Rev. Lett.* **110**, 084101, (2013).